

# Hard Exudate Detection using Local Texture Analysis and Gaussian Processes.

Adrián Colomer<sup>1\*</sup>, Pablo Ruiz<sup>2</sup>, Valery Naranjo<sup>1</sup>, Rafael Molina<sup>3</sup>, and Aggelos K. Katsaggelos<sup>2</sup>

<sup>1</sup> Instituto de Investigación e Innovación en Bioingeniería (I3B),  
Universitat Politècnica de València, Camino de Vera s/n, 46022, Valencia, Spain.  
<sup>2</sup> Dpt. of Electrical Engineering and Computer Science, Northwestern University.  
<sup>3</sup> Dpto. de Ciencias de la Computación e I.A., Universidad de Granada, Granada,  
Spain  
`adcogra@upv.es`

**Abstract.** Exudates are the most noticeable sign in the first stage of diabetic retinopathy. This disease causes about five percent of world blindness. Making use of retinal fundus images, exudates can be detected, which helps the early diagnosis of the pathology. In this work, a novel method for automatic hard exudate detection is presented. After an exhaustive pre-processing step, Local Binary Patterns Variance (LBPV) histograms are used to locally extract texture information. We then use Gaussian Processes to distinguish between healthy and pathological retinal patches. The proposed methodology is validated using the *E-OPHTA exudates* database. The experimental results demonstrate that Gaussian Process classifiers outperform the current state of the art classifiers for this problem.

**Keywords:** Hard Exudate, Local Binary Patterns, Gaussian Processes, Bayesian Modeling, Variational Inference.

## 1 Introduction

Diabetic Retinopathy (DR) causes about five percent of world blindness and signs of this eye disease are found in around 33% of the diabetes population [1]. There exist two types of DR: Non-Proliferative and Proliferative Diabetic Retinopathy [2]. Non-Proliferative DR is the earliest stage of the pathology and it is characterized by deposits of extra fluid and small amounts of blood, from the vessels into the retina, called exudates and microaneurysms/hemorrhages (Fig. 1a).

---

\* This work has been supported in part by the Ministerio de Economía y Competitividad under contracts DPI2016-77869-C2-{1,2}-R, and the Department of Energy grant DE-NA0002520. The work of Adrián Colomer has been supported by the Spanish FPI Grant BES-2014-067889. We gratefully acknowledge the support of NVIDIA Corporation with the donation of the Titan Xp GPU used for this research.

RGB fundus images are acquired by a retinal camera using non-invasive protocols. This kind of images is commonly used by ophthalmologists to diagnose diabetic retinopathy. Exudates are revealed as yellow whitish areas of random size and shape generated by the accumulation of fats and lipids. As these lesions are the most noticeable sign of non-proliferative diabetic retinopathy, indicating the first stage of the disease, the exudate detection is a key step in the early diagnosis of the pathology. Due to the large population at risk of DR, there exists the need of developing automatic algorithms able to discriminate regions where exudates are present.

Fundus databases contain images with different resolutions, non-uniform illumination, reflects and noise or artefacts (Figs. 1b and 1c), due to the uncalibrated conditions in the acquisition process. Besides these problems, the physiological properties of the retina produce other image variabilities such as highlights near the vessels, characteristic of young retinas (Fig. 1d), and different fundus colour depending on age, ethnicity, retina pigmentation and other anatomical human factors (Fig. 1e). In most of the state-of-the-art works, conflictive images are removed from the original dataset when proposed algorithms are evaluated [3]. However, a computer-aided diagnose system must deal with the high variability among fundus images, so we will not eliminate problematic images.

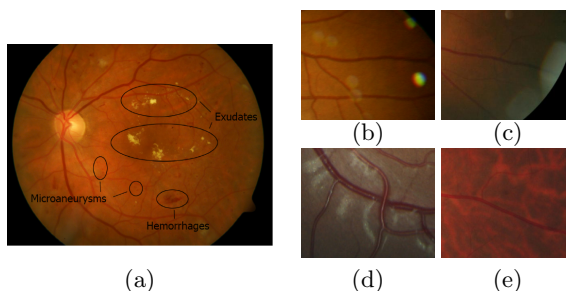


**Fig. 1.** (a) Noisy image, (b) Image with reflects, (c) Highlighted retina, (d) Tessellated image due to ethnicity.

In the literature, the most common procedure to detect exudates exploits their shape information. In [4–6], exudates are segmented by applying mathematical morphology and thresholding techniques. Another common way to detect these lesions is to extract global information from the fundus images and identify the unhealthy regions through supervised or unsupervised classification techniques [3, 7, 8].

The main contribution of this work is the validation of a new methodology to distinguish between healthy and pathological retinal tissues. Our methodology is based on local texture analysis and makes use of Gaussian Processes for Classification (GPC). To the best of our knowledge, in the literature to detect exudates, features have only been extracted from the whole image and local features and GPs have not been used before for exudate detection. A comparison

with the most commonly used classification methods for solving this problem is also carried out.

The rest of the paper is organized as follows: in Section 2 the fundus image pre-processing is detailed. Then, in Section 3 the local texture analysis method is described. Section 4 details the Variational Gaussian Process for classification approach. Finally, Section 5 provides the experimental validation and in Section 6 conclusions and some future work directions are reported.

## 2 Fundus image pre-processing

As mentioned in Section 1, databases usually contain images with different resolutions propitiating that some structures and lesions are not comparable. The first preprocessing step aims to normalize the image dimensions following the method described in [9].

Blood vessels are considered as noise or artefacts that hamper the classification of pathologies based on background textures. The contribution of these structures to the texture descriptor must be removed. In this work, diffusion-based inpainting techniques [10] are applied to eliminate the vascular tree.

Another factor that contributes to the heterogeneity of fundus databases is the difference among background colours. This fact is due to the particular physiological properties of each human's retina. With the aim of developing a system invariant to high-lighted retinas and tessellated images, a colour normalization is carried out. Geometric transformations to the chromatic histogram (plane r-g) are performed taking into account a reference image with the ideal background colour [11].

After these steps, the green channel of the RGB fundus images is selected (Fig. 2b) because this component maximizes the contrast between lesions and background [6].

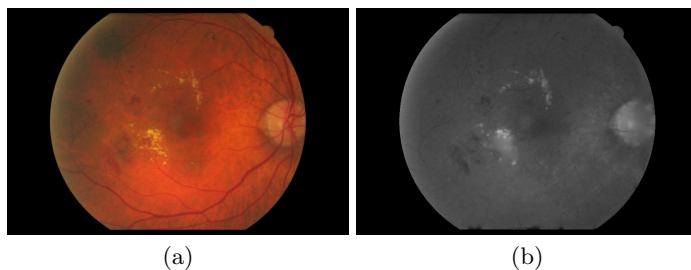


**Fig. 2.** (a) Original image and (b) Green component of the pre-processed image.

## 3 Local texture analysis

Local Binary Patterns (LBP) is a grey-scale texture descriptor. The basic LBP version assigns a label to each pixel  $(i, j)$  taking into account its neighbourhood

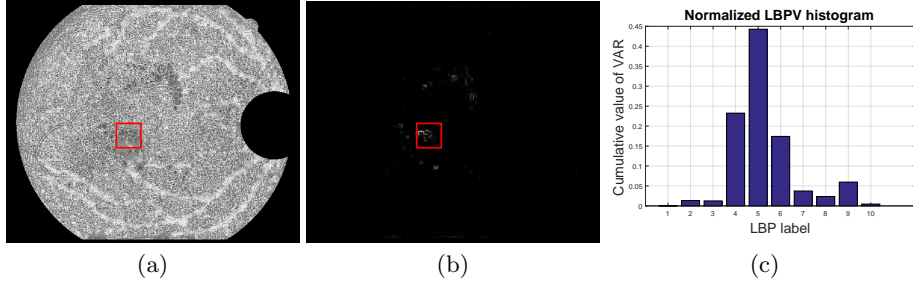


**Fig. 3.** Local texture analysis. (a) LBP and (b) VAR image with different highlighted patches and (c) the LBPV normalized histogram computed for the yellow patch.

as follows:

$$LBP_{P,R}(i, j) = \sum_{p=0}^{P-1} s(g_p - g_c) \cdot 2^p, \quad s(x) = \begin{cases} 1 & \text{if } x \geq 0 \\ 0 & \text{if } x < 0 \end{cases} \quad (1)$$

where  $P$  represents the number of samples on the symmetric circular neighbourhood of radius  $R$ ,  $g_c$  is the gray value of pixel  $(i, j)$  and  $g_p$  the gray value of each neighbour.

Although many variants of LBP exist in the literature, due to the properties of the rotation-invariant uniform (riu2) LBP presented in [12], we use it in this work to encode a selected subset of patterns. When LBP is used for texture description it is common to additionally include a contrast measure by defining the Rotational Invariant Local Variance (VAR) as:

$$VAR_{P,R}(i, j) = \frac{1}{P} \sum_{p=0}^{P-1} (g_p - \mu)^2, \quad \mu = \frac{1}{P} \sum_{p=0}^{P-1} g_p \quad (2)$$

Lesions due to diabetic retinopathy vary in size depending on the stage of the disease. In most cases, lesions represent less than one percent of the total number of pixels in the retinal fundus image. For this reason, the texture descriptor is applied locally to obtain relevant features for a large variety of images.

The LBP and VAR images, both of dimensions  $M_1 \times M_2$ , are extracted from the green channel of the preprocessed original image. These resulting images are divided into patches using a sliding window and normalized histograms are computed for each patch taking into account the information provided by both images (Fig. 3). LBP variance (LBPV) histogram [13] accumulates the VAR value for each LBP label inside the window according to the following equation:

$$LBPV_{P,R}(k) = \sum_{i=1}^{M_1} \sum_{j=1}^{M_2} w(LBP_{P,R}(i, j), k), \quad k \in [0, K] \quad (3)$$

$$w(LBP_{P,R}(i,j), k) = \begin{cases} VAR_{P,R}(i,j), & LBP_{P,R}(i,j) = k \\ 0, & otherwise. \end{cases} \quad (4)$$

where  $K$  is the maximal LBP label.

The window used to compute the local histograms is a  $b \times b$  square with overlap of  $(\Delta x, \Delta y)$ . Note that patches containing optic disk pixels [14] are not considered in the process. Patches should also be completely contained within the field of view of the retinal image.

## 4 Variational Gaussian Process for Classification

Let  $\mathbf{X} = [\mathbf{x}_1, \dots, \mathbf{x}_N]^t$  be the matrix containing the samples, where each  $\mathbf{x}_i \in \mathbb{R}^K$  is the descriptor for the  $i$ -th patch, calculated as described in Section 3,  $N$  is the number of patches used for training, and  $K$  is the number LBPV features. Let  $\mathbf{y} \in \{0, 1\}^N$  be the vector of labels, where 1 refers to ‘‘pathologic patches’’ and 0 refers to ‘‘healthy patches’’.

To model the relationship between samples and labels, the GPC formulation [15] introduces a latent variable  $\mathbf{f} \in \mathbb{R}^N$ , which is in fact a prior on the functions over the feature space. This latent variable has the following Gaussian prior distribution

$$p(\mathbf{f}|\Omega) = \mathcal{N}(\mathbf{f}|\mathbf{0}, \mathbf{K}), \quad (5)$$

where  $\mathbf{K}$  is the covariance matrix, which depends on a set of parameters  $\Omega$  to be estimated and has the form  $\mathbf{K}_{ij} = \mathbf{k}(\mathbf{x}_i, \mathbf{x}_j)$  where  $\mathbf{k}(\cdot, \cdot)$  is a kernel function (see [15]).  $\mathbf{K}$  is the way in which GPs exploit the correlation between samples, since each  $\mathbf{K}_{ij}$  is calculated by evaluating a kernel function (an inner product in a transformed vector space) on the samples  $\mathbf{x}_i$  and  $\mathbf{x}_j$ . Although  $\mathbf{K}$  depends on  $\mathbf{X}$ , we have removed it from dependencies in  $p(\mathbf{f}|\Omega)$  for simplicity.

The relationship between  $\mathbf{f}$  and the labels  $\mathbf{y}$  is modeled by the so-called logistic likelihood function

$$p(\mathbf{y}|\mathbf{f}) = \prod_{i=1}^N p(y_i|f_i) = \prod_{i=1}^N \left( \frac{1}{1 + e^{-f_i}} \right)^{y_i} \left( \frac{1}{1 + e^{f_i}} \right)^{1-y_i}. \quad (6)$$

Notice that for large positive values of  $f_i$ ,  $p(y_i = 1|f_i) \approx 1$ , and for negative values of  $f_i$  with large absolute value  $p(y_i = 1|f_i) \approx 0$ .

The joint distribution of  $\mathbf{y}$ ,  $\mathbf{f}$ , and  $\Omega$  is

$$p(\mathbf{y}, \mathbf{f}, \Omega) = p(\mathbf{y}|\mathbf{f})p(\mathbf{f}|\Omega)p(\Omega). \quad (7)$$

where we have used a flat improper prior for  $\Omega$ .

Since  $p(\mathbf{f}, \Omega|\mathbf{y})$  can not be calculated, we resort to the mean field approximation [16] and solve the problem

$$\hat{\mathbf{q}}(\mathbf{f}), \hat{\mathbf{q}}(\Omega) = \arg \min_{\mathbf{q}(\mathbf{f}), \mathbf{q}(\Omega)} \int \mathbf{q}(\mathbf{f})\mathbf{q}(\Omega) \ln \frac{\mathbf{q}(\mathbf{f})\mathbf{q}(\Omega)}{p(\mathbf{y}, \mathbf{f}, \Omega)} d\mathbf{f}d\Omega, \quad (8)$$

where  $\hat{q}(\Omega)$  is restricted to be a degenerate distribution, to finally obtain  $p(\mathbf{f}, \Omega | \mathbf{y}) \approx \hat{q}(\mathbf{f})\hat{q}(\Omega)$ , see [17] for details.

Unfortunately eq. (8) can not be evaluated due to the functional form of the likelihood function in eq. (6). To alleviate this problem we use the lower bound provided in [17],

$$\begin{aligned} \log p(\mathbf{y} | \mathbf{f}) &\geq \log \mathbf{H}(\mathbf{y}, \mathbf{f}, \boldsymbol{\xi}) = \\ &\mathbf{f}^t (\mathbf{y} - \frac{1}{2} \mathbf{1}) - \mathbf{f}^t \mathbf{A} \mathbf{f} + \boldsymbol{\xi}^t \mathbf{A} \boldsymbol{\xi} + \frac{1}{2} \boldsymbol{\xi}^t \mathbf{1} - \sum_{i=1}^N \log(1 + e^{\xi_i}), \end{aligned} \quad (9)$$

where  $\boldsymbol{\xi} = (\xi_1, \dots, \xi_N)^t$  is a set of nonnegative parameters to be estimated,  $\mathbf{A} = \text{diag}(\lambda(\xi_1), \dots, \lambda(\xi_N))$ , with  $\lambda(\xi) = \frac{1}{2\xi}(\frac{1}{1+e^{-\xi}} - \frac{1}{2})$ , and  $\mathbf{1}$  is a column vector with all components equal to 1.

The joint distribution in eq. (7) can then be lower bounded as  $p(\mathbf{y}, \mathbf{f}, \Omega) \geq \mathbf{M}(\mathbf{y}, \mathbf{f}, \Omega, \boldsymbol{\xi}) = \mathbf{H}(\mathbf{y}, \mathbf{f}, \boldsymbol{\xi})p(\mathbf{f} | \Omega)p(\Omega)$ , which produces

$$\begin{aligned} &\int q(\mathbf{f})q(\Omega) \ln \frac{q(\mathbf{f})q(\Omega)}{p(\mathbf{y}, \mathbf{f}, \Omega)} d\mathbf{f}d\Omega \\ &\leq \min_{\boldsymbol{\xi} \geq \mathbf{0}} \int q(\mathbf{f})q(\Omega) \log \frac{q(\mathbf{f})q(\Omega)}{\mathbf{M}(\mathbf{y}, \mathbf{f}, \Omega, \boldsymbol{\xi})} d\mathbf{f}. \end{aligned} \quad (10)$$

Let  $\boldsymbol{\xi}^k$  be the current value of  $\boldsymbol{\xi}$ , then

$$\begin{aligned} &\min_{q(\mathbf{f})} \int q(\mathbf{f}) \log \frac{q(\mathbf{f})}{\mathbf{M}(\mathbf{y}, \mathbf{f}, \Omega, \boldsymbol{\xi}^k)} d\mathbf{f} = \text{const} \\ &- \ln \mathcal{N} \left( \frac{1}{2} (\mathbf{y} - \frac{1}{2} \mathbf{1}) | \mathbf{0}, \frac{1}{2} \mathbf{A}^k + \mathbf{A}^k \mathbf{K}_\Omega \mathbf{A}^k \right) \end{aligned} \quad (11)$$

which produces  $\Omega^k$ , the current estimate of the vector where  $\hat{q}(\Omega)$  is degenerate,

$$\Omega^k = \arg \max_{\Omega} \mathcal{N} \left( \frac{1}{2} (\mathbf{y} - \frac{1}{2} \mathbf{1}) | \mathbf{0}, \frac{1}{2} \mathbf{A}^k + \mathbf{A}^k \mathbf{K}_\Omega \mathbf{A}^k \right). \quad (12)$$

Fixing  $\boldsymbol{\xi}$  to  $\boldsymbol{\xi}^k$  and  $\Omega$  to  $\Omega^k$  we obtain

$$q^k(\mathbf{f}) = \mathcal{N}(\langle \mathbf{f} \rangle_k, \boldsymbol{\Sigma}_k) \quad (13)$$

where  $\langle \mathbf{f} \rangle_k = \boldsymbol{\Sigma}_k (\mathbf{y} - \frac{1}{2} \mathbf{1})$  and  $\boldsymbol{\Sigma}_k = (\mathbf{K}_{\Omega^k}^{-1} + 2\mathbf{A}^k)^{-1}$ . Finally, solving

$$\boldsymbol{\xi}^{k+1} = \max_{\boldsymbol{\xi}} \langle \ln \mathbf{M}(\mathbf{y}, \mathbf{f}, \Omega^k, \boldsymbol{\xi}) \rangle_{q^k(\mathbf{f})} \quad (14)$$

we obtain

$$\xi_i^{k+1} = \sqrt{\langle f_i \rangle^2 + \boldsymbol{\Sigma}_k(i, i)}. \quad (15)$$

In Algorithm 1 we summarize the estimation procedure.

---

**Algorithm 1** Learning Algorithm
 

---

**Require:** Initial  $\xi^1 = \mathbf{1}$  and  $k = 1$ .

- 1: **repeat**
  - 2:   Calculate  $\Omega^k$  using  $\xi^k$  in eq. (12).
  - 3:   Calculate  $q^k(\mathbf{f})$  using  $\Omega^k$  and  $\xi^k$  in eq. (13) .
  - 4:   Calculate  $\xi^{k+1}$  using  $q^k(\mathbf{f})$  and  $\Omega^k$  in eq. (15).
  - 5:    $k = k + 1$
  - 6: **until** convergence
- 

Given a new patch  $\mathbf{x}_*$  we would like to calculate

$$\begin{aligned} p(y_*|\mathbf{y}) &= \int_{f_*} p(y_*|f_*) \left( \int_{\mathbf{f}} p(f_*|\mathbf{f})p(\mathbf{f}|\mathbf{y})d\mathbf{f} \right) df_* \\ &\approx \int_{f_*} p(y_*|f_*) \left( \int_{\mathbf{f}} p(f_*|\mathbf{f})\hat{q}(\mathbf{f})d\mathbf{f} \right) df_*, \end{aligned} \quad (16)$$

where the approximated posterior  $\hat{q}(\mathbf{f})$  has been calculated, at convergence, in Algorithm 1, and  $p(y_*|f_*)$  is given by eq. (6). The conditional distribution  $p(f_*|\mathbf{f})$  can be calculated from eq. (5) as

$$p(f_*|\mathbf{f}) = \mathcal{N}(f_*|\mathbf{h}^t\mathbf{K}^{-1}\mathbf{f}, c - \mathbf{h}^t\mathbf{K}^{-1}\mathbf{h}), \quad (17)$$

with  $\mathbf{h} = (\mathbf{k}(\mathbf{x}_*, \mathbf{x}_1), \dots, \mathbf{k}(\mathbf{x}_*, \mathbf{x}_N))^t$ ,  $c = \mathbf{k}(\mathbf{x}_*, \mathbf{x}_*)$ . The probability that patch  $\mathbf{x}_*$  belongs to class “pathological” can be written then as

$$p(y_* = 1|\mathbf{y}) \approx \int \frac{1}{1 + e^{-f_*}} \mathcal{N}(f_*|m(f_*), v^2(f_*))df_*, \quad (18)$$

with  $m(f_*) = \mathbf{h}^t\mathbf{K}^{-1}\langle\mathbf{f}\rangle$  and  $v^2(f_*) = c - \mathbf{h}^t(\mathbf{K} + (2\mathbf{A})^{-1})^{-1}\mathbf{h}$ . The integral in eq. (18) is approximated as in [17], to obtain

$$p(y_* = 1|\mathbf{y}) \approx \left( 1 + \exp \left\{ -m(f_*)(1 + \frac{1}{8}\pi v^2(f_*))^{-1/2} \right\} \right)^{-1}. \quad (19)$$

As can be observed in Fig. 2a, pathological areas represent only a small region of the whole image, which results in a very unbalanced dataset. Training a classifier with an unbalanced dataset can produce overfitting to the majority class “healthy” [18]. To avoid this problem we proceed as follows. Let us assume that the number of healthy samples is  $T$  times the number of pathological ones, then the set of all healthy samples is partitioned into  $T$  subsets with the same cardinality as the number of pathological samples. A committee of  $T$  GPCs is then learned with training sets formed by joining all pathological training samples and each partition of healthy training samples. Soft majority voting is used as the final criterion. If the obtained probability is higher than a given threshold  $\delta$ , the patch is assigned to the class “pathological”. Notice that this is not a bagging procedure [19], since sampling is not uniform and with replacement.

## 5 Experimental Results

To validate the proposed methodology, the *E-OPHTHA exudates* public database [20] was selected. This database is composed by a large variety of images with different resolutions containing tessellations, round spots, brights near the blood vessels, reflects. The performance of our algorithm was tested using the forty seven pathological images and their corresponding ground truth manually annotated by experts. From these forty seven pre-processed images, healthy and pathological patches are extracted as explained in Section 3 using  $b = 64$  and  $(\Delta x, \Delta y) = (32, 32)$ . Afterwards, LBPV normalized histograms are computed for  $LBP_{8,1}^{riu2}$  obtaining  $K = 10$  features from each patch.

In addition to validating the proposed methodology, we also compared it to both, baseline and the state-of-the-art algorithms, for the hard exudate detection problem. The baseline method is Linear Support Vector Machine (LIN-SVM) with a Linear kernel [21], while the state-of-the-art methods are SVM with Radial Basis Function (RBF) kernel [21] and Random Forest (RF) [22].

RBF kernel is also used for GPC. Unlike GPC, SVM and RF do not provide estimation methods for their respective parameters. To perform a fair comparison, cross-validation is used to set the “cost” and “length-scale” parameters in SVM, and “number of trees” in RF.

To avoid biased results produced by training and testing sets selection, in this work we use a leave-one-out cross-validation procedure. The whole dataset with 47 images is divided into 5 partitions, (3 with 9 images, and 2 with 10 images). Then patches in 4 partitions are used for training a classifier as described in Section 4, and the remaining patches are used for testing. The procedure is carried out 5 times, leaving out a different partition in each repetition. Since the testing set is also unbalanced, for each classifier we select the decision threshold  $\delta$  obtaining the best trade-off between sensitivity and specificity.

The mean numeric results for GPC are reported in Table 1, where 0.7840, 0.7840, 0.7833, and 0.6044 of accuracy (Acc.), sensitivity (Sens.), specificity (Spec.) and Matthews correlation coefficient (MCC) [23] are obtained, respectively. The mean numerical results for LIN-SVM, RBF-SVM and RF methods are also reported in Table 1. We can observe that GPC obtains the best result with respect to all metrics of performance. For AUC, GPC is almost 2% better than RF and RBF-SVM, and 4% than the baseline method LIN-SVM. For accuracy, sensitivity, and specificity, GPC is approximately 1%, 2%, and 4% better than RF, RBF-SVM, and LIN-SVM, respectively.

The mean ROC curve for GPC is plotted in red in Fig. 4a, which obtains a 0.8645 of Area Under ROC Curve. Based on [24], the proposed methodology can be considered a “good diagnostic test” for the hard exudate detection. Mean ROC curves for LIN-SVM, RBF-SVM and RF methods are also plotted in Fig. 4a. We can observe that GPC obtains a better performance than all of them for both, high and low false positive rates. RF works better than RBF-SVM for low false positive rates, however RBF-SVM obtains better results than RF for high false positives rates. Figure 4b shows the exudate detection results in a representative image of *E-OPHTHA* database.

	Acc.	Sens.	Spec.	AUC	MCC
<b>LIN-SVM</b>	0.7481	0.7475	0.7471	0.8299	0.4292
<b>RBF-SVM</b>	0.7642	0.7625	0.7635	0.8447	0.4718
<b>RF</b>	0.7701	0.7741	0.7687	0.8473	0.5275
<b>GPCs</b>	<b>0.7840</b>	<b>0.7840</b>	<b>0.7833</b>	<b>0.8645</b>	<b>0.6044</b>

**Table 1.** Figures of merit for the compared methods.

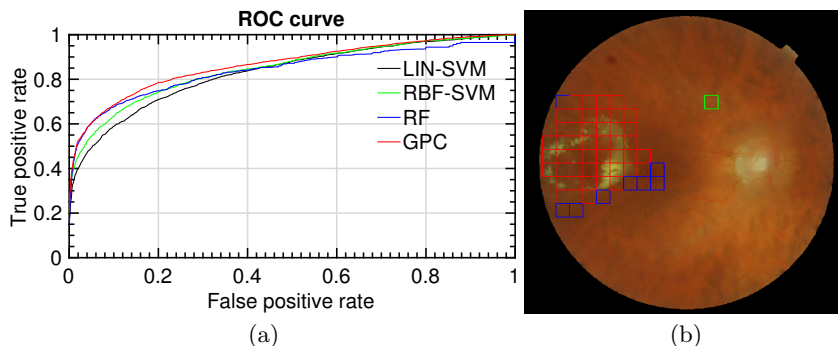


**Fig. 4.** (a) ROC curves for the compared methods and (b) exudate detection using GPCs in a representative image (TP in red, FP in green and TN in blue).

## 6 Conclusions

In this paper, we presented a system, based on local texture analysis and Gaussian Processes, to detect exudates for DR diagnosis. Local texture description allows to identify pathological tissue providing robustness against the high fundus image variability and spatial information of the lesions. The obtained ROC curves provide evidence that GPCs result in the best classification solution independently of the decision threshold. The proposed methodology outperforms the current state of the art algorithms, namely RBF-SVM and RF. Future work will deal with the detection of dark lesions in order to develop a computer-aided diagnosis system for automatic DR detection. In addition, other texture descriptors will be explored to improve the classification results.

## References

1. World Health Organization (WHO): Universal eye health: a global action plan 2014-2019. Technical report (2015)
2. American Academy of Ophthalmology (AAO) Retina/Vitreous Panel: Preferred Practice Pattern® Guidelines. Diabetic Retinopathy, San Francisco, CA (2016)
3. Morales, S., Engan, K., Naranjo, V., Colomer, A.: Retinal disease screening through local binary patterns. *IEEE Journal of Biomedical and Health Informatics* **21**(1) (Jan 2017) 184–192

4. Welfer, D., Scharcanski, J., Marinho, D.R.: A coarse-to-fine strategy for automatically detecting exudates in color eye fundus images. *Computerized Medical Imaging and Graphics* **34**(3) (2010) 228 – 235
5. JayaKumari, C., Maruthi, R.: Detection of hard exudates in color fundus images of the human retina. *Procedia Engineering* **30** (2012) 297 – 302 International Conference on Communication Technology and System Design 2011.
6. Walter, T., Klein, J.C., Massin, P., Erginay, A.: A contribution of image processing to the diagnosis of diabetic retinopathy - detection of exudates in color fundus images of the human retina. *IEEE Trans. Med. Imaging* **21**(10) (2002) 1236–1243
7. Karegowda, A.G., Nasiha, A., Jayaram, M.A., Manjunath, A.S.: Article: Exudates detection in retinal images using back propagation neural network. *International Journal of Computer Applications* **25**(3) (July 2011) 25–31
8. Sopharak, A., Dailey, M.N., Uyyanonvara, B., et al.: Machine learning approach to automatic exudate detection in retinal images from diabetic patients. *Journal of Modern Optics* **57**(2) (2010) 124–135
9. Zhang, X., Thibault, G., et al.: Spatial normalization of eye fundus images. In: *ISBI 2012 : 9th IEEE International Symposium on Biomedical Imaging, IEEE* (2012)
10. Guillemot, C., Le Meur, O.: Image inpainting: Overview and recent advances. *IEEE Signal Processing Magazine* **31**(1) (2014) 127–144
11. Colomer, A., Naranjo, V., Angulo, J.: Colour normalization of fundus images based on geometric transformations applied to their chromatic histogram. In: *2017 IEEE International Conference on Image Processing (ICIP)*. (Sept 2017) 3135–3139
12. Ojala, T., Pietikainen, M., Maenpaa, T.: Multiresolution gray-scale and rotation invariant texture classification with local binary patterns. *IEEE Transactions on Pattern Analysis and Machine Intelligence* **24**(7) (2002) 971–987
13. Guo, Z., Zhang, L., Zhang, D.: Rotation invariant texture classification using {LBP} variance (lbpv) with global matching. *Pattern Recognition* **43**(3) (2010) 706 – 719
14. Morales, S., Naranjo, V., Angulo, J., Alcaniz, M.: Automatic detection of optic disc based on pca and mathematical morphology. *Medical Imaging, IEEE Transactions on* **32**(4) (2013) 786–796
15. Rasmussen, C.E., Williams, C.K.I.: *Gaussian processes for machine learning. Adaptive computation and machine learning.* MIT Press, Cambridge, Mass (2006)
16. Parisi, G.: *Statistical Field Theory.* Edicin: New edition edn. Perseus Books, Reading, Mass (1998)
17. Bishop, C.: *Pattern Recognition and Machine Learning.* Edicin: 1st ed. 2006. corr. 2nd printing 2011 edn. Springer, New York (February 2010)
18. Tapia, S.L., Molina, R., Blanca, N.P.d.l.: Detection and localization of objects in Passive Millimeter Wave Images. In: *2016 24th European Signal Processing Conference (EUSIPCO)*. (August 2016) 2101–2105
19. Breiman, L.: Bagging predictors. *Machine Learning* **24**(2) (August 1996) 123–140
20. Decencière, E., Cazuguel, G., Zhang, X., et al.: Teleophta: Machine learning and image processing methods for teleophthalmology. *{IRBM}* **34**(2) (2013) 196 – 203
21. Cristianini, N., Shawe-Taylor, J.: *An Introduction to Support Vector Machines and Other Kernel-based Learning Methods.* Cambridge University Press (2000)
22. Breiman, L.: Random Forests. *Machine Learning* **45**(1) (October 2001) 5–32
23. Matthews, B.: Comparison of the predicted and observed secondary structure of t4 phage lysozyme. *Biochimica et Biophysica Acta (BBA) - Protein Structure* **405**(2) (1975) 442 – 451
24. Swets, J.A.: Measuring the accuracy of diagnostic systems. *Science* **240**(4857) (1988) 1285–1293